RSC Advances

PAPER

View Article Online
View Journal | View Issue

Cite this: *RSC Adv.*, 2022, **12**, 12957

Structural and anionic effects of microcrystalline Zn-CPs on 4-nitrophenol sensing performances†

Hyemin Lee,[a] Min-Yeong Kim *[b] and Haeri Lee *[a]

Received 24th February 2022
Accepted 24th April 2022

DOI: 10.1039/d2ra01239a

rsc.li/rsc-advances

Coordination polymers (CPs: $[ZnL_3]_n(X)_{2n}$, L = *trans*-1,4-bis(imidazolyl)-2-butene; $X^- = BF_4^-$, ClO_4^-, NO_3^-) allow for detection of the 4-nitrophenol (4-NP) oxidation process by enhanced electrochemical signals. Electrochemical measurement is a highly sensitive method providing much evidence of chemical reactions on an electrode surface. In the present study, we designed and synthesized, with reference to X-ray diffraction data and by spectroscopic analyses, new 3D coordination structures containing imidazolyl donors and zinc(II). The presence of microcrystals $[ZnL_3]_n(BF_4)_{2n}$ on the working electrode enhanced the redox signals. Therefore, we propose a simple catalytic process that can explain these results and clarify the influence of anions that constitute CP materials used to improve electrochemical detection applications. The CP materials were characterized by nuclear magnetic resonance (NMR), infrared spectroscopy (IR), thermogravimetric (TG) analyses, single crystal X-ray diffraction (SC-XRD), and electrochemical analyses.

Introduction

A self-assembly process between metal cations and electron-donor ligands allows for construction of coordination compounds and introduction of functions at the molecular level.[1–3] Network structures by control of building blocks and relatively large voids usually have been reported as resulting in metal–organic frameworks (MOFs) and coordination polymers (CPs) boasting the structural advantages such as high thermal stability, molecular rigidity, and specific hydrophilicity of voids.[4] Many research groups have reported useful coordination compounds for gas adsorption,[5] chiral molecule detection,[6] and catalysis.[7] Even though many MOFs have rather low electrical conductivity, are unstable in aqueous solution and fragile in their coordination bonds, some efforts to apply them as electrocatalysts have been made, given their unique advantages such as the possibility of molecular adsorption of sensing targets and redox mediators in a single molecule.[8,9]

The need for detection of hazardous substances in environmental samples has increased significantly in recent years.[10,11] 4-Nitrophenol (4-NP), albeit a toxic chemical, has been used in a wide range of industries such as synthetic dyes, pharmaceuticals, petrochemicals, herbicides, pesticides, and explosives.[12] Due to its high persistence in nature, 4-NP highly accumulates in ecosystems, impacting harmfully on plants, animals, and humans, even at low concentrations.[13,14] Therefore, there has been a great demand for the detection and analysis. According to the literature, detection of 4-NP has been performed by various analytical techniques such as high-performance liquid chromatography (HPLC), fluorescence detection,[15–17] electrophoresis, and electrochemical method.[18,19] However, those techniques are rather expensive and require highly trained operators to treat samples. On the other hand, the electrochemical method, which is receiving plenty attention in the field of real-time monitoring, is not only simple to operate and low-cost, but also has excellent sensitivity.[20–22]

Recently, various materials, including carbon composites, metal oxides, and others, have been studied as electrochemical catalysts for nitrophenol detection.[23–28] However, the use of metal complexes for construction electrochemical electrodes, notwithstanding the exciting opportunities they present in various fields, is still in its infancy.[29,30] So far, research on electrochemical detection of 4-NP *via* the phenol oxidation process is even less reported. For detection of 4-NP, electroreduction reaction mainly has been performed; phenol functional groups, though, can be oxidized at higher positive potentials.[31] During the oxidation process, 4-nitrophenoxy radicals and 4-nitrophenoxy cations are sequentially formed, and then polymeric species from those monomers are assembled on the electrode surface through their coupling reaction, which produces evident electrode fouling.[32] To solve this problem, in the present study, a low-cost disposable screen-printed carbon electrode (SPCE) was applied to an *in situ* electrochemical sensing method in real time.

Zinc(II) itself is redox-inactive, but we assumed Zn-CPs to work as a platform for 4-NP oxidation reaction. Also, control of

[a]*Department of Chemistry, Hannam University, Daejeon, 34054, Republic of Korea. E-mail: haeri.lee@hnu.ac.kr*

[b]*Department of Electrochemistry, Korea Institute of Materials Science (KIMS), Changwon, 51508, Republic of Korea. E-mail: kmy4820@kims.re.kr*

† Electronic supplementary information (ESI) available. CCDC 2143359–2143361. For ESI and crystallographic data in CIF or other electronic format see https://doi.org/10.1039/d2ra01239a

structural dimensions and anionic effects of CP structures are very interesting in an understanding of the structure–property relationship point of view. Therefore, three zinc(II) coordination compounds were synthesized and used for 4-NP sensing. New zinc(II)-organic compounds were synthesized and their crystal structures were characterized by single-crystal XRD (Scheme 1). Self-assembly of zinc(II) pseudo halides (ZnX_2; $X^- = BF_4^-$, ClO_4^-) and nitrogen donor ligands (**L**, *trans*-1,4-bis(imidazolyl)-2-butene) gave rise to 3-fold interpenetrated frameworks, $[Zn\mathbf{L}_3]_n(BF_4)_{2n}$ and $[Zn\mathbf{L}_3]_n(ClO_4)_{2n}$, showing polyatomic anions aligned in a columnar fashion in the 1D void channel structure. The physicochemical properties were analyzed by IR spectra, thermogravimetric/differential scanning calorimetry (TG/DSC) analyses, and X-ray crystallography. Then, their microcrystals were deposited on the electrode for an applicability study of the direct electrochemical sensing effect. $[Zn\mathbf{L}_3]_n(BF_4)_{2n}$ showed good electrochemical catalytic performance for the 4-NP oxidation reaction. Additionally, to investigate the structural effect on sensing properties, a 2D-sheet structure of $[Zn_2(NO_3)_4\mathbf{L}_3]_n$ was prepared.

Experimental

Materials and measurements

Chemicals including *trans*-1,4-dibromobutene and imidazole were purchased from TCI-SejinCI and zinc(II) precursors, potassium chloride (KCl), $[Fe(CN)_6]^{3-}$, $[Fe(CN)_6]^{4-}$, Nafion (5 wt%), and 4-NP were obtained from Merck. All were used without further purification. 400 MHz ^{1}H NMR spectra were recorded on a Varian Mercury Plus. Infrared (IR) spectra were obtained by a Fourier Transform Infrared Spectroscopy (FT-IR, [Transmittance mode], Thermo Fischer Scientific, UK; Nicolet iS10), samples having been prepared as KBr pellets. Thermal analyses were carried out at KBSI Pusan center under an N_2 atmosphere at a scan rate of 10 °C min^{-1} using SDT Q600. SC-XRD data on $[Zn\mathbf{L}_3]_n(BF_4)_{2n}$, and $[Zn_2(NO_3)_4\mathbf{L}_3]_n$ were collected on a Bruker SMART APEX II coated with Paraton-*N* oil under a stream of N_2 gas at 120 K. Diffraction data for $[Zn\mathbf{L}_3]_n(ClO_4)_{2n}$ were obtained on the 2D beamline at Pohang Accelerator Laboratory (PAL) in South Korea. Zn-CP morphology was studied under field-emission scanning electron microscopy (FE-SEM) (SUPRA40, Zeiss, Germany). The chemical shift and surface properties of Zn-CP were investigated using X-ray photoelectron spectroscopy (XPS, Multilab 2000, Thermo Fisher Scientific) with an Al Kα source, and XRD (D/max-2500/PC, Rigaku, Japan). The electrochemical catalytic properties were studied by cyclic voltammetry (CV), electrochemical impedance spectroscopy (EIS), and square wave voltammetry (SWV) (KST P-2, Kosentech, Republic of Korea). For the 4-NP sensor, an SPCE based on a three-electrode system consisting of a carbon working electrode (0.0196 cm^2), a carbon counter electrode and a Ag reference electrode, and were fabricated (BTI, Republic of Korea). A 1 M HCl solution containing 0.25 M $FeCl_3$ was dropped onto the silver layer and reacted for 30 minutes

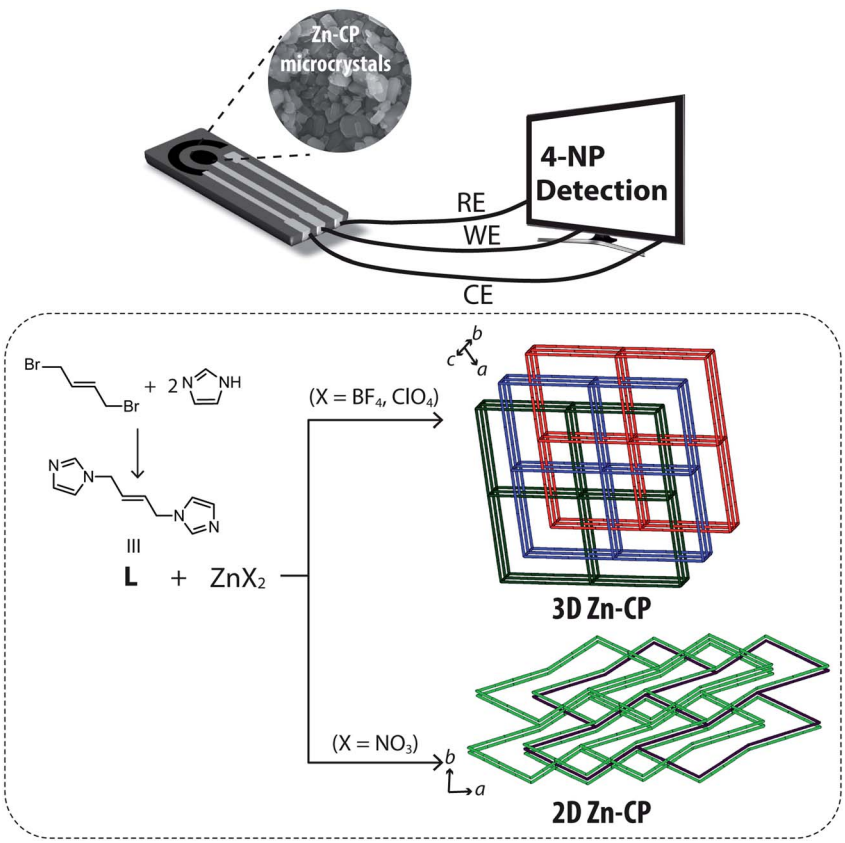

Scheme 1 Synthetic procedure for **L** and zinc(II)-CP architectures; electrochemical responses by Zn-CP-modified electrodes.

before being washed as with the distilled water (DI) water to prepare an Ag/AgCl layer.

Preparation of *trans*-1,4-bis(imidazolyl)-2-butene (L)

A mixture of imidazole (3.4 g, 50 mmol) and *trans*-1,4-dibromobutene (2.1 g, 10 mmol) in chloroform (100 mL) was refluxed for 5 h with vigorous stirring. The organic layer was washed with saturated $NaHCO_3$ solution three times. After drying the organic layer using anhydrous magnesium sulfate, the chloroform was evaporated with a rotary evaporator. The product was obtained as a pale-yellow crystalline solid in 28% yield (0.53 g). Mp 70 °C. Decomposition temp. 245 °C. ^{1}H NMR (400 MHz, DMSO-d_6) δ 7.59 (s, 2H), 7.10 (s, 2H), 6.89 (s, 2H), 5.73 (m, 2H), 4.61 (d, J = 4.4 Hz, 4H); ^{13}C NMR (75 MHz, Me_2SO-d_6): δ = 136.99, 129.04, 128.41, 119.20, 46.82. IR (KBr pellet, cm^{-1}): $\tilde{\nu}$ = 3106 (m), 2922 (s), 2851 (w), 1675 (w) 1504 (s), 1228 (s), 1078 (m), 1025 (w), 907 (m), 738 (m), 621 (m). High-resolution ESI-MS: m/z 189.1140 (calcd for $[C_{10}H_{12}N_2 + H^+]^+$ = 189.1140).

Preparation of $[ZnL_3]_n(BF_4)_{2n}$

A dichloromethane solution (6 mL) of **L** (2.7 mg, 15 μmol) was slowly added to an acetone solution (6 mL) of zinc(II) tetrafluoroborate (1.2 mg, 5 μmol). After 3 days, colorless crystals of $[ZnL_3]_n(BF_4)_{2n}$ were obtained in a 65% yield (2.6 mg). Mp 321 °C (dec.). IR (KBr pellet, cm^{-1}): $\tilde{\nu}$ = 3434 (br), 1517 (m), 1384 (w), 1277 (w), 1234 (m), 1084 (s, BF_4^-), 935 (m), 836 (w), 739 (m), 660 (m).

Preparation of $[ZnL_3]_n(ClO_4)_{2n}$

This product was prepared in the same manner as $[ZnL_3]_n(BF_4)_{2n}$, using $Zn(ClO_4)_2$ instead of $Zn(BF_4)_2$ in a 71% yield (2.9 mg). Mp 262 °C (dec.). IR (KBr pellet, cm^{-1}): $\tilde{\nu}$ = 3421 (br), 3131 (m), 2941 (w), 1607 (w), 1514 (m), 1276 (m), 1232 (m), 1096 (s, ClO_4^-), 100 (m), 835 (m), 739 (m), 5622 (m).

Preparation of $[Zn_2(NO_3)_{4L3}]_n$

A dichloromethane solution (4 mL) of **L** (5.4 mg, 30 μmol) was slowly added to an acetone solution (4 mL) of zinc(II) nitrate (5.8 mg, 20 μmol). After 3 days, colorless crystals of $[Zn_2(NO_3)_{4L3}]_n$ in a 47% yield (8.9 mg) after 3 days. Mp 315 °C (dec.). IR (KBr pellet, cm^{-1}): $\tilde{\nu}$ = 3434 (br), 3135 (m), 2338 (w), 1617 (w), 1496 (m), 1479 (m), 1384 (m), 1307 (m, NO_3^-), 1105 (m), 655 (m).

X-ray crystallography

Single crystals for X-ray structural analyses of $[ZnL_3]_n(BF_4)_{2n}$ and $[Zn_2(NO_3)_{4L3}]_n$ were collected on a Bruker APEX III coated with Paraton-*N* oil at 100 K. Data were collected in-house on a Bruker PHOTON II equipped with an INCOATEC microfocus sealed tube (IμS 3.0) using Mo K_α. The resolution was cut off at 0.80 Å for $[ZnL_3]_n(BF_4)_{2n}$, and at 0.77 Å for $[Zn_2(NO_3)_{4L3}]_n$, after which the signal-to-noise ratio had dropped below $I/\sigma(I) < 2.0$. The data were integrated with APEX III. For $[ZnL_3]_n(ClO_4)_{2n}$, diffraction data were obtained on the 2D beamline at PAL.[33] Diffraction data were collected by a Rayonix MX225HS CCD area detector controlled by the PAL BL2D-SMDC Program.[34] HKL3000sm was used for cell refinement and data reduction.[35] The structures were resolved by intrinsic phasing/direct methods using SHELXT[36] and refined with SHELXL (2018/3)[37] for full-matrix least-squares routines on F^2 and ShelXle[38] as a graphical user interface.

Fabrication of Zn-CP electrodes

Homogeneously dispersed Zn-CP (1.0 mg mL^{-1} of $[ZnL_3]_n(BF_4)_{2n}$, $[ZnL_3]_n(ClO_4)_{2n}$, $[Zn_2(NO_3)_{4L3}]_n$) was prepared in distilled water and Nafion (v/v = 1 : 0.1). Before modification on the electrode, the SPCE was sonicated in distilled water and ethanol for 5 min, respectively. Then, 1 μL of Zn-CP dispersion solution was drop-casted onto the SPCE working electrode, dried for 6 h, and used for subsequent electrochemical measurement analyses.

Preparation of natural water samples

To demonstrate the utilitarian potential of our sensors, they were tested in various real samples by standard analytical methods. Prior to the analysis, the prepared water samples were filtered three times through a 10 μm filter. Various amounts of 4-NP were spiked into them, and then the evaluated detection performance of the 4-NP sensor was evaluated.

Results and discussion

Synthesis and spectroscopic characterization of L and Zn-CP

Trans-1,4-bis(imidazolyl)-2-butene (**L**) was obtained from the reaction between *trans*-1,4-dibromobutene and imidazole in chloroform, as shown in Scheme 1. **L** was analyzed by ^{1}H, ^{13}C, COSY, and NOESY spectra (Fig. S1–S4, ESI†). According to the thermogravimetric analysis, **L** was stable up to 245 °C (Fig. S5, ESI†). High-resolution ESI-mass data showed that $[C_{10}H_{12}N_2 + H^+]^+$ = 189.1140 (calcd 189.1140) as major ionized species in a positive mode (Fig. S6, ESI†). Self-assembly of zinc(II) pseudo halides (ZnX_2, X^- = ClO_4^-, BF_4^-) and **L** gave rise to 3D coordination polymers, $[ZnL_3]_n(ClO_4)_{2n}$ and $[ZnL_3]_n(BF_4)_{2n}$, which were analyzed by X-ray crystallographic analysis. The IR spectra showed typical molecular vibrations of polyatomic anions at 1096 cm^{-1} for $[ZnL_3]_n(ClO_4)_{2n}$, and 1084 cm^{-1} for $[ZnL_3]_n(BF_4)_{2n}$, with specific molecular vibrational information of the ligands in the fingerprint region (Fig. S7, ESI†). As shown in Fig. S8, ESI,† the thermal stabilities of the compounds were similar: the decomposition temperatures of 262 °C for $[ZnL_3]_n(ClO_4)_{2n}$ and 321 °C for $[ZnL_3]_n(BF_4)_{2n}$ were higher than for free **L** (245 °C).

Crystal structures

All of the crystal structures were obtained by slow addition of an acetone solution of ZnX_2 (X^- = BF_4^-, ClO_4^-, NO_3^-) to a dichloromethane solution of **L** (Table 1). The crystal structure of $[ZnL_3]_n(BF_4)_{2n}$ was built as a **pcu** net (point symbol $4^{12}6^3$) showing 3-fold interpenetrated frameworks (Fig. 1a). In the packing structure, BF_4^- anions are positioned in one dimensional (1D) channels in the (001) direction. $[ZnL_3]_n(ClO_4)_{2n}$ is the iso-structure with $[ZnL_3]_n(BF_4)_{2n}$ except with polyatomic

Table 1 Crystallographic data for $[ZnL_3]_n(BF_4)_{2n}$, $[ZnL_3]_n(ClO_4)_{2n}$, and $[Zn_2(NO_3)_{4L3}]_n$

	$[ZnL_3]_n(BF_4)_{2n}$	$[ZnL_3]_n(ClO_4)_{2n}$	$[Zn_2(NO_3)_{4L3}]_n$
CCDC no.	2143359	2143360	2143361
Empirical formula	$C_{30}H_{36}B_2F_8N_{12}Zn$	$C_{30}H_{36}Cl_2N_{12}O_8Zn$	$C_{15}H_{18}N_8O_6Zn$
Formula weight	803.7	828.98	471.74
Temperature (K)	173(2)	173(2)	173(2)
Wavelength (Å)	0.71073	0.650	0.71073
Crystal system	Trigonal	Trigonal	Triclinic
Space group	$P\bar{3}$	$P\bar{3}$	$P\bar{1}$
a (Å)	12.1766(12)	12.3005(17)	8.4896(4)
b (Å)	12.1766(12)	12.3005(17)	8.6765(5)
c (Å)	6.9569(11)	6.7310(14)	14.6410(7)
α (°)	90	90	87.742(2)
β (°)	90	90	89.147(2)
γ (°)	120	120	83.008(2)
Volume	893.3(2)	882.0(3)	1069.55(9)
Z	1	1	2
Density (calculated) (Mg m^{-3})	1.494	1.561	1.465
Absorption coefficient (mm^{-1})	0.771	0.717	1.196
$F(000)$	412	428	484
Crystal size (mm^3)	0.086 × 0.025 × 0.023	0.052 × 0.024 × 0.022	0.286 × 0.059 × 0.058
Theta range for data collection (°)	2.928 to 26.996	1.748 to 26.991	2.367 to 26.500
Index ranges	$-11 \leqq h \leqq 15, -15 \leqq k \leqq 15, -8 \leqq l \leqq 8$	$-17 \leqq h \leqq 17, -17 \leqq k \leqq 17, -9 \leqq l \leqq 9$	$-10 \leqq h \leqq 10, -10 \leqq k \leqq 10, -18 \leqq l \leqq 18$
Reflections collected	7371	9150	37136
Independent reflections	1295 [R(int) = 0.0694]	1687 [R(int) = 0.0897]	4319 [R(int) = 0.0796]
Completeness	99.10%	99.80%	97.30%
Absorption correction	Semi-empirical from equivalents	Empirical	Semi-empirical from equivalents
Max. and min. transmission	1.000 and 0.789	1.000 and 0.944	1.000 and 0.789
Refinement method	Full-matrix least-squares on F^2	Full-matrix least-squares on F^2	Full-matrix least-squares on F^2
Data/restraints/parameters	1295/0/90	1687/0/81	4319/0/272
Goodness-of-fit on F^2	1.109	1.155	1.07
Final R indices [I > 2sigma (I)]	$R1 = 0.0599$, w$R2 = 0.1245$	$R1 = 0.0424$, w$R2 = 0.1167$	$R1 = 0.0397$, w$R2 = 0.1029$
R indices (all data)	$R1 = 0.0755$, w$R2 = 0.1319$	$R1 = 0.0440$, w$R2 = 0.1178$	$R1 = 0.0420$, w$R2 = 0.1052$
Largest diff. peak and hole (e $Å^{-3}$)	1.043 and −0.316	1.082 and −0.927	0.958 and −0.580

anions occupying the voids. As shown in Fig. 1a, the geometry of zinc(II) is an octahedral, binding six nitrogen atoms from six ligands (Zn–N = 2.192(3) Å for $[ZnL_3]_n(BF_4)_{2n}$ and 2.1949(13) Å for $[ZnL_3]_n(ClO_4)_{2n}$). The closest distance between the zinc(II) atoms sitting in the neighboring polymers is 6.95(1) and 6.73(1) Å for $[ZnL_3]_n(BF_4)_{2n}$ and $[ZnL_3]_n(ClO_4)_{2n}$, respectively. In order to differentiate skeletal structures by control of the binding affinity of counter anions, zinc(II) nitrate ($Zn(NO_3)_2$) was applied for self-assembly: NO_3^- is a stronger coordinative polyatomic anion compared to BF_4^- and ClO_4^-. The reaction of $Zn(NO_3)_2$ and **L** produced a 2D network structure, $[Zn_2(NO_3)_{4L3}]_n$ (Fig. 1d). The coordination atmosphere around zinc(II) in $[Zn_2(NO_3)_{4L3}]_n$ was three nitrogen atoms from three ligands in equatorial positions along with two oxygen atoms from anions, thereby showing a distorted trigonal bipyramid geometry (Fig. 1a). Interestingly, NO_3^- anions blocked off the axial positions for extension of the structure to 3D; therefore, the structure remained 2D rather than 3D. The 2D network structure consists of M_6L_6 ring composites showing a honeycomb topology. The contact voids were calculated as 130.69 $Å^3$ (14.6% for $[ZnL_3]_n(BF_4)_{2n}$), 125.76 $Å^3$ (14.3%, for $[ZnL_3]_n(ClO_4)_{2n}$) and 118.14 $Å^3$ (11.0%, for $[Zn_2(NO_3)_{4L3}]_n$). Pores of $[ZnL_3]_n(BF_4)_{2n}$, and $[ZnL_3]_n(ClO_4)_{2n}$ contain their counter anions (BF_4^- or ClO_4^-, respectively), while solvents are filled in $[Zn_2(NO_3)_{4L3}]_n$ pores (Fig. 1b and d).

Electrochemical properties of Zn-CPs

Zinc(II) coordination compounds in the solid state offer an advantage for adoption of stable zinc(II) catalytic sites on electrodes, while zinc(II) salts such as $Zn(BF_4)_2$, $Zn(ClO_4)_2$, and $Zn(NO_3)_2$ are highly soluble in aqueous solution, which is the media necessary for cyclovoltammetric analysis. To investigate the electrochemical catalytic performance of Zn-CP for 4-NP oxidation, SPCE working electrodes were prepared by drop-casting 10–20 μm microcrystals dispersed in water (Fig. S9, ESI†). The bulk crystalline solid samples were examined according to their powder XRD patterns (Fig. S10, ESI†). The electron transport behaviors of the redox couple at the $[ZnL_3]_n(BF_4)_{2n}$, $[ZnL_3]_n(ClO_4)_{2n}$, and $[Zn_2(NO_3)_{4L3}]_n$ electrodes were studied using the CV technique in 5 mM $[Fe(CN)_6]^{3-/4-}$ with 0.1 M KCl solution at various scan rates from 25 to 300 mV s^{-1} (Fig. 2). The redox peak current (anodic (I_{pa}) and cathodic (I_{pc})

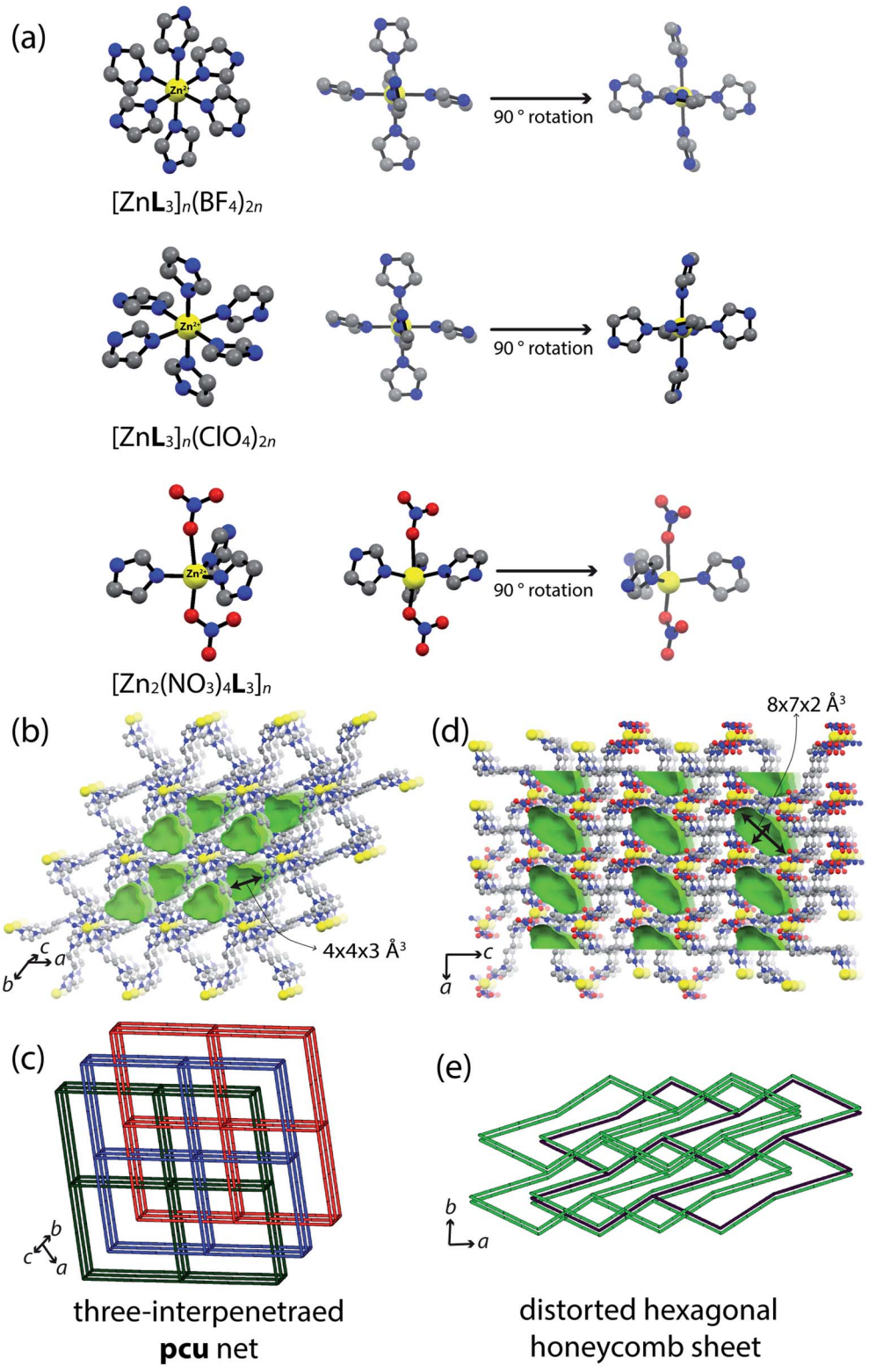

Fig. 1 Images showing detailed geometries around Zn(II) (a), a packing structure (b) and topological analysis for $[ZnL_3]_n(X)_{2n}$ (X = ClO_4 or BF_4) (c), an extended structure (d) and topological analysis for $[Zn_2(NO_3)_{4L3}]_n$ (e).

peak currents) increased with the increasing scan rate for all of the electrodes. The peak current ratio of I_{pa} and I_{pc} was approximately 1 at 100 mV s^{-1}, which indicates that the redox quasi-reversible of the Zn-CP electrodes is good. The inset plots of the square roots of the scan rate ($v^{1/2}$) *versus* the redox peak currents show that the peak current had a linear relationship

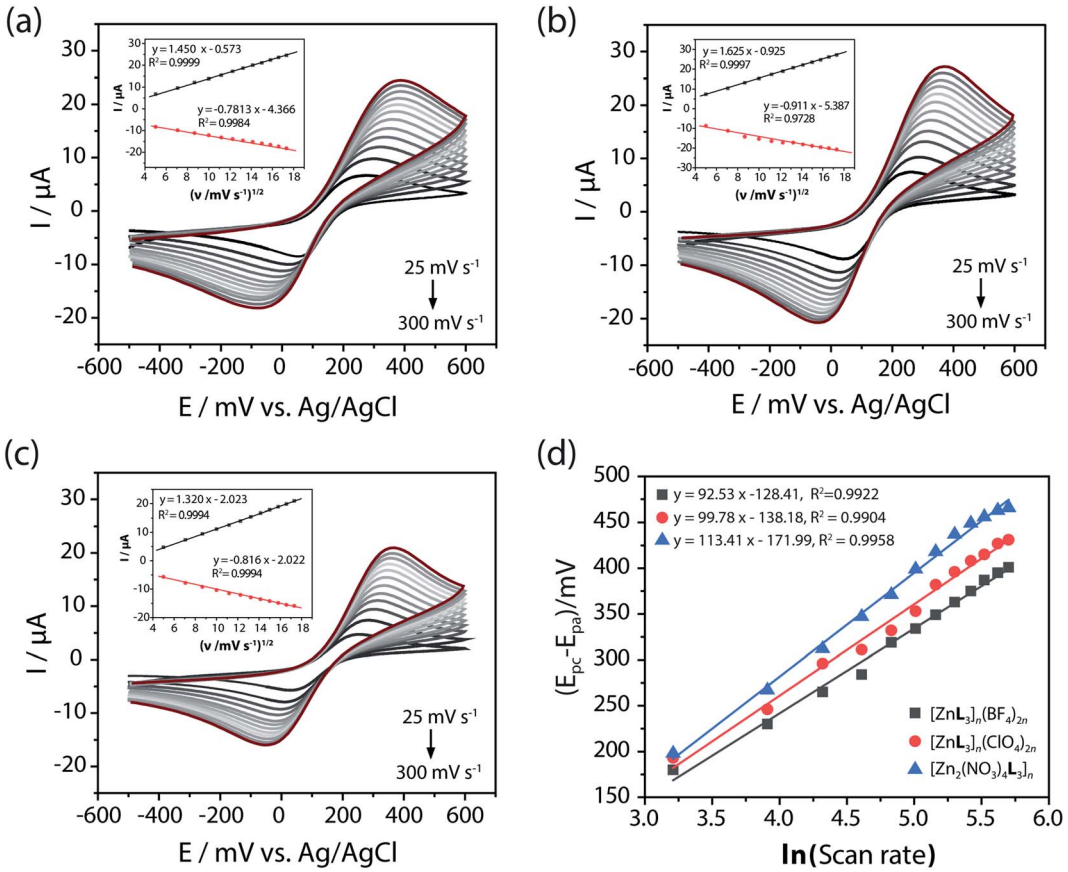

Fig. 2 Electrochemical behaviors of Zn-CP electrodes: $[ZnL_3]_n(ClO_4)_{2n}$ (a), $[ZnL_3]_n(BF_4)_{2n}$ (b), and $[Zn_2(NO_3)_4L_3]_n$ (c), and peak-to-peak separation between anodic and cathodic peaks for each electrode (d).

with the square roots of the scan rates. This indicates that the redox process is a diffusion-controlled electrochemical process. The Randles–Sevcik equation (eqn (1)) is useful to describe how the scan rate affects the peak current depending on other electrochemical parameters such as concentrations and diffusional properties. As shown in the insets in Fig. 2a–c, the peak current (I_p) extends linearly with the square root of the scan rate at the three electrodes.

$$I_{pa} = (2.69 \times 10^5)n^{2/3}AD^{1/2}\nu^{1/2}C^{o} \quad (1)$$

where, n = number of electrons in the redox reaction, ν = scan rate in V s^{-1}, F = Faraday's constant 96 485 coulombs $mole^{-1}$, A = electroactive surface area in cm^2, R = gas constant 8.314 J $mole^{-1}$ K^{-1}, T = temperature in K, D = diffusion coefficient of analyte in cm^2 s^{-1}, C^o = bulk concentration of the redox probe in molarity.[39] This is generally for diffusion-limited electrochemical reactions at planar electrodes, where the current is determined by the rate of diffusion of the reacting species to the electrode surface. Moreover, the Randles–Sevcik equation was used to estimate an approximate value of the electro-active surface area of the Zn-CP electrode. Accordingly, A was calculated to be 6.28 mm^2. As shown in Fig. 2d, for all three electrodes, the peak-to-peak difference (ΔE_p) of the cathode and anode potential peaks clearly increases as the scan rate increases. That the ΔE_p value of the $[Zn_2(NO_3)_{4L3}]_n$-modified electrode increases at a high rate implies a slow kinetics of charge transfer within the electrode. In a comparative experiment on the electron transport behaviors of the bare, $[ZnL_3]_n(BF_4)_{2n}$, $[ZnL_3]_n(ClO_4)_{2n}$, and $[Zn_2(NO_3)_{4L3}]_n$ electrodes, the current responses of the $[ZnL_3]_n(BF_4)_{2n}$ and $[ZnL_3]_n(ClO_4)_{2n}$ electrodes were higher than that of the bare-SPCE, while that of the $[Zn_2(NO_3)_{4L3}]_n$ electrode showed a significantly weak response due to the instability of the solid state of $[Zn_2(NO_3)_{4L3}]_n$ in water media (Fig. S11, ESI†).

The electrochemical properties of the Zn-CPs were investigated by EIS. The EIS results based on 0.1 M KCl containing 5 mM $[Fe(CN)_6]^{3-/4-}$ for the Zn-CP-modified electrodes are plotted in Fig. 3. The charge transfer resistance of a material in the EIS data refers to the diameter of the semicircle: the smaller the diameter is, the lower the charge transfer resistance of materials is. Herein, the $[Fe(CN)_6]^{3-/4-}$ complex ion is used as an electron transport rate probe to characterize the electrode surface. The diameters are shown in the order of $[Zn_2(NO_3)_{4L3}]_n$, $[ZnL_3]_n(ClO_4)_{2n}$, $[ZnL_3]_n(BF_4)_{2n}$, and bare SPCE. The relative equivalent circuits (inset of Fig. 3) and R_p values of these Zn-CP-modified electrodes are followings: because of the low electrical conductivity of Zn-CP, the R_p values of the three Zn-CP electrodes were larger in which of the bare electrode (0.33 kΩ). Here, it is interesting to note that the electrode modified by

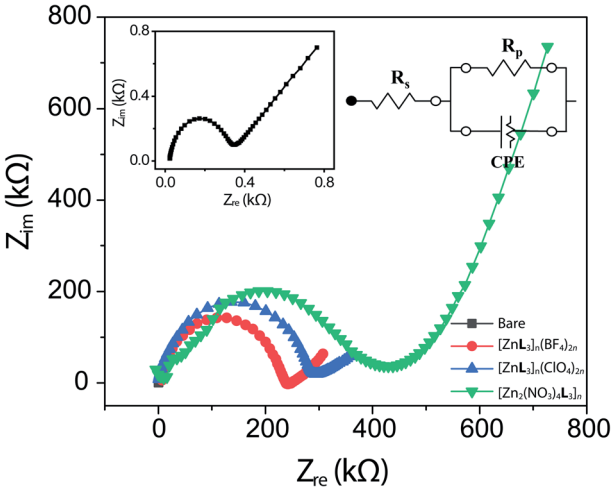

Fig. 3 EIS of Zn-CP-modified electrodes $[ZnL_3]_n(BF_4)_{2n}$ (red), $[ZnL_3]_n(ClO_4)_{2n}$ (blue), and $[Zn_2(NO_3)_4L_3]_n$ (green), and bare electrode (black) and a relative equivalent circuit for the Zn-CP-modified electrodes. Inset: relative equivalent circuits.

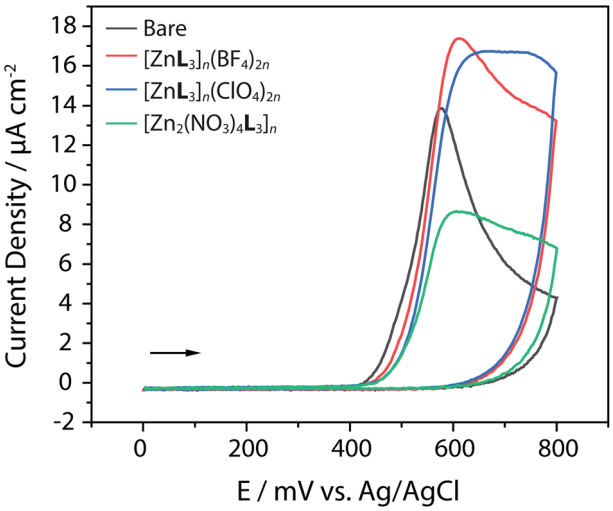

Fig. 4 Electrochemical responses in 4-NP detection using the electrode without any modification (black) and modified electrodes using $[ZnL_3]_n(BF_4)_{2n}$ (red), $[ZnL_3]_n(ClO_4)_{2n}$ (blue), and $[Zn_2(NO_3)_4L_3]_n$ (green).

$[ZnL_3]_n(BF_4)_{2n}$ (476 k kΩ) had a smaller R_p value relative to the were larger than that of the bare electrode (0.335 kΩ). Here, it is interesting to note that the $[ZnL_3]_n(BF_4)_{2n}$ (241 kΩ), and $[ZnL_3]_n(ClO_4)_{2n}$ (283 kΩ) electrodes. This was owed to the fact that the anion electrically coupled to the CP affected the conductivity of the CP.

As is well known, for Zn(II), the spin polarization is not modified by the coordination environment, due to the d^{10} configuration. In addition, it is generally reported that the Zn coordination compounds exhibit neutral charge in their structures. On the other hand, our proposed 3D Zn-CPs consist of Zn(II) and neutral ligands, which remain as cationic skeletal structures. With infinite electrostatic interactions, the anions (BF_4^- and ClO_4^-) were successfully trapped in the 3D structure. On the other hand, $[Zn_2(NO_3)_4L_3]_n$-modified electrode showed the lowest electrochemical response because of its low stability which drove the solvation of compounds in water and break its skeletal structure during electrochemical data collection. Therefore, electrochemical sensing performance improvement was attempted by utilizing the combination effect of the positive and negative ions. It is believed that the electrochemical reaction between the sensor probe and the analyte was improved by promoting electron transfer through electron localization caused by the binding of anion possessing abundant electrons even without significant enhancement of the electrochemically active site by the reasons of spin polarization or porous structure.

Sensing properties for 4-NP oxidation

4-NP detection has been studied by various analytical techniques (Table 2). In this work, electrochemical oxidation of 4-NP on Zn-CP-modified electrodes was adopted. The oxidation current intensity on the surface of Zn-CP electrodes in 0.1 M PBS (pH 7.0) containing 5 mM 4-NP were obtained as a single oxidation, indicating 4-NP oxidation is an irreversible process. As shown in Fig. 4, among the three modified electrode, $[ZnL_3]_n(BF_4)_{2n}$ and $[ZnL_3]_n(ClO_4)_{2n}$ showed higher 4-NP oxidation current peaks than did the bare electrode, suggesting that Zn-CP exhibits the 4-NP oxidation catalytic effect. To the best of our knowledge, 4-NP oxidation displayed an irreversible reaction at pH 7.[39,40] Therefore, we proposed mechanism for 4-NP oxidation: the oxidative product of 4-NP is 4-nitrosophenol through phenolate radical formation showing a strong oxidation peak at +0.6 V (Fig. S12, ESI†).

Table 2 Technical comparison of reported analytical methods for 4-NP detection

Analytical techniques	Dynamic range (μg mL^{-1})	Detection limit (μg mL^{-1})	Ref.
IP-SAME[a]-HPLC	0.0002–0.075	0.0001	23
SPME[b]-HPLC-UV	0.01–30	0.0036	24
Fluorescence	0.051–13.7	0.026	25
Fluorescence	0.139–0.695	0.0062	26
Electrochemical reduction	0.014–16.68	0.00278	27
Electrochemical reduction	0.083–4.448	0.0072	28
Electrochemical oxidation	1.39–973	0.528	This work

[a] IP-SAME: ion pair based surfactant-assisted microextraction. [b] SPME: solid-phase microextraction.

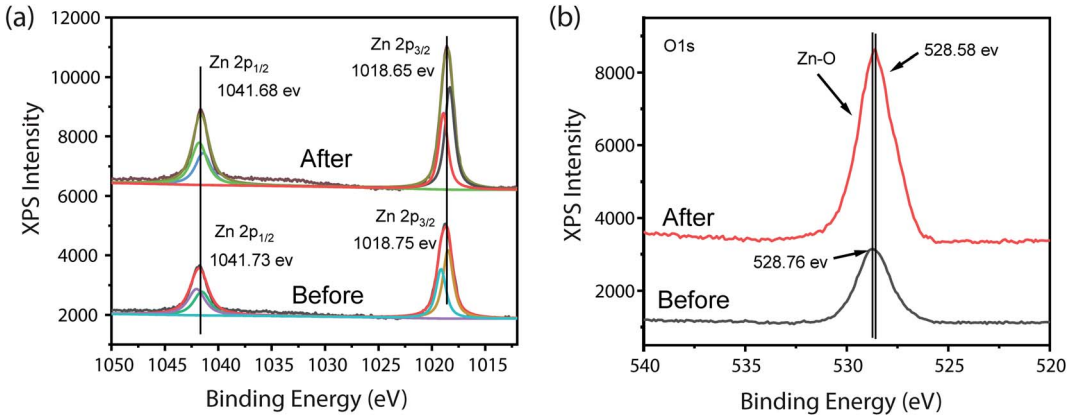

Fig. 5 XPS data of $[ZnL_3]_n(BF_4)_{2n}$-modified electrode, before and after electrochemical reaction of 4-NP oxidation; Zn 2p (a), O 1s (b).

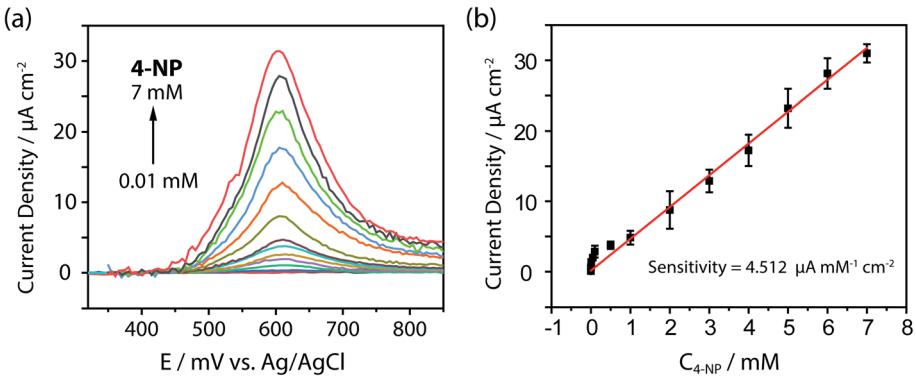

Fig. 6 Electrochemical detection of 4-NP using $[ZnL_3]_n(BF_4)_{2n}$ microcrystalline electrode, SWV curves (a), calibration plot (b).

To elucidate the chemical integrity of Zn-CP before and after 4-NP oxidation reaction, the oxidation state of $[ZnL_3]_n(BF_4)_{2n}$-modified electrode were examined by XPS. All samples were completely dried before measurements. As shown Fig. 5, there are no significant changes in binding energy observed in XPS before and after 4-NP oxidation. Merely, the intensity of O 1s (Zn–O) peak increased after the 4-NP oxidation regarding the possibility of more Zn–O content after 4-NP oxidation.

Subsequent experiments using $[ZnL_3]_n(BF_4)_{2n}$ (which showed the best performance) with square-wave voltammetry (SWV) analysis were carried out to determine the sensitivity and limit of detection (LOD). Fig. 6a plots the SWV curves in the 4-NP concentration range of 0.01 mM–7 mM and sensitivity 4.512 μA mM^{-1} cm^{-2}, and Fig. 6b displays the corresponding calibration plot. The LOD was calculated as 3.8 μM (0.528 ppm). These results notably show that Zn-CPs can be directly applied as catalysts for electrochemical sensors. Although the LOD is not as low as in other recent fields and studies incorporating MOFs and composites, the present as-synthesized Zn-CP electrode showed – due to the influence of anions in channels – a wider

Table 3 Electrochemical determination of 4-NP concentration in natural-water samples

Environmental samples[a]	Added (μM)	Found (μM)	Recovery %	RSD % ($n = 3$)
River water	5.0	4.78	95.6	4.21
	50.0	47.64	95.3	2.65
	100.0	95.14	95.14	1.13
Reservoir water	5.0	5.37	107.4	3.36
	50.0	53.21	106.4	2.23
	100.0	104.74	104.7	0.78
Lake water	5.0	4.86	97.2	3.97
	50.0	48.29	96.6	3.54
	100.0	96.47	96.47	1.18

[a] River water: Nakdong River in Miryang; reservoir water: Daega reservoir in Goseong; lake water: Yongji lake in Changwon.

linear range for 4-NP detection. These results will be able to guide further 4-NP-detection application studies on the utility of other Zn-CP-modified SPCE/functional material composites.

Applications for 4-NP sensing in natural-water media

The direct detection of 4-NP from natural-water samples is rather difficult due to the low concentrations of substrates. On the other hand, the weak electrochemical signals of 4-NP oxidation using the $[Zn\mathbf{L}_3]_n(BF_4)_{2n}$ electrode is relatively sensitive enough for detection of low substrate concentration. After the addition of 5.0, 50.0, and 100.0 μM of 4-NP to natural-water samples, the 4-NP concentrations were calculated with reference to the electrochemical signals from the $[Zn\mathbf{L}_3]_n(BF_4)_{2n}$ electrode, respectively (Table 3). In addition, the recovery percentage of the oxidized phenol group of 4-NP revealed that oxidized 4-NP was 95.3–107.4% recovered with acceptable RSD values, which suggests that Zn-CP is applicable as an electrode material. Therefore, electrochemical oxidation of the phenolic group of 4-NP can be considered to be suitable for electrochemical sensor application and suggests that Zn-CP is directly applicable as an electrode material.

Conclusions

3D Zn-CP structures containing imidazolyl donor ligands were obtained in high yields. Their stable metal–organic architectures in the solid state could be directly utilized for sensing of a toxic substrate, namely 4-NP. Furthermore, detection and estimation of 4-NP concentrations in several types of natural-water samples were successfully carried out, which results reflected a high potential for hybrid inorganic–organic electrode materials. However, the electrical conductivity and LOD of the Zn-CP-modified electrodes were not sufficient relative to the results obtained in recent studies. Therefore, integration of Zn-CPs with other functional materials is required in future studies. As far as we currently know, we are the first to have determined and understood the effect of anions on electrochemical sensing in their electrostatic binding to Zn-CP in the cationic backbone. At the very last, the present study provides an exciting new perspective for researchers interested in employing Zn-CPs in next-generation electrochemical sensors.

Conflicts of interest

There are no conflicts to declare.

Acknowledgements

This work was supported by 2021 the Hannam University Research Fund. H. Lee thanks to Dr Dongwook Kim from Institute of Basic Science (IBS) for data collection of X-ray diffraction and discussions.

References

1 G. F. Huo, X. Shi, Q. Tu, Y. X. Hu, G. Y. Wu, G. Q. Yin, X. Li, L. Xu, H. M. Ding and H. B. Yang, Radical-Induced Hierarchical Self-Assembly Involving Supramolecular Coordination Complexes in Both Solution and Solid States, *J. Am. Chem. Soc.*, 2019, **141**, 16014–16023.
2 Y. Domoto, M. Abe, T. Kikuchi and M. Fujita, Self-Assembly of Coordination Polyhedra with Highly Entangled Faces Induced by Metal–Acetylene Interactions, *Angew. Chem., Int. Ed.*, 2020, **59**, 3450–3454.
3 L. Wang, B. Song, Y. Li, L. Gong, X. Jiang, M. Wang, S. Lu, S. Lu, X. Q. Hao, Z. Xia, Y. Zhang, Y. Zhang, S. W. Hla and X. Li, Self-Assembly of Metallo-Supramolecules under Kinetic or Thermodynamic Control: Characterization of Positional Isomers Using Scanning Tunneling Spectroscopy, *J. Am. Chem. Soc.*, 2020, **142**, 9809–9817.
4 H. C. J. Zhou and S. Kitagawa, Metal-Organic Frameworks (MOFs), *Chem. Soc. Rev.*, 2014, **43**, 5415–5418.
5 H. Furukawa, N. Ko, Y. B. Go, N. Aratani, S. B. Choi, E. Choi, A. Ö. Yazaydin, R. Q. Snurr, M. O'Keeffe, J. Kim and O. M. Yaghi, Ultrahigh Porosity in Metal-Organic Frameworks, *Science*, 2010, **329**, 424–428.
6 H. Jiang, K. Yang, X. Zhao, W. Zhang, Y. Liu, J. Jiang and Y. Cui, Highly Stable Zr(IV)-Based Metal-Organic Frameworks for Chiral Separation in Reversed-Phase Liquid Chromatography, *J. Am. Chem. Soc.*, 2021, **143**, 390–398.
7 H. Huang, K. Shen, F. Chen and Y. Li, Metal–Organic Frameworks as a Good Platform for the Fabrication of Single-Atom Catalysts, *ACS Catal.*, 2020, **10**, 6579–6586.
8 H.-F. Wang, L. Chen, H. Pang, S. Kaskel and Q. Xu, MOF-derived electrocatalysts for oxygen reduction, oxygen evolution and hydrogen evolution reactions, *Chem. Soc. Rev.*, 2020, **49**, 1414–1448.
9 G. Skorupskii, B. A. Trump, T. W. Kasel, C. M. Brown, C. H. Hendon and M. Dincă, Efficient and tunable one-dimensional charge transport in layered lanthanide metal–organic frameworks, *Nat. Chem.*, 2020, **12**, 131–136.
10 M. A. La Merrill, L. N. Vandenberg, M. T. Smith, W. Goodson, P. Browne, H. B. Patisaul, K. Z. Guyton, A. Kortenkamp, V. J. Cogliano, T. J. Woodruff, L. Rieswijk, H. Sone, K. S. Korach, A. C. Gore, L. Zeise and R. T. Zoeller, Consensus on the key characteristics of endocrine-disrupting chemicals as a basis for hazard identification, *Nat. Rev. Endocrinol.*, 2020, **16**, 45–57.
11 T. K. Kasonga, M. A. A. Coetzee, I. Kamika, V. M. Ngole-Jeme and M. N. Benteke Momba, Endocrine-disruptive chemicals as contaminants of emerging concern in wastewater and surface water: A review, *J. Environ. Manage.*, 2021, **277**, 111485.
12 P. Balasubramanian, T. S. T. Balamurugan, S.-M. Chen and T.-W. Chen, Simplistic synthesis of ultrafine CoMnO3 nanosheets: An excellent electrocatalyst for highly sensitive detection of toxic 4-nitrophenol in environmental water samples, *J. Hazard. Mater.*, 2019, **361**, 123–133.
13 R. Nehru, P. K. Gopi and S.-M. Chen, Enhanced sensing of hazardous 4-nitrophenol by a graphene oxide–TiO 2 composite: environmental pollutant monitoring applications, *New J. Chem.*, 2020, **44**, 4590–4603.

14 Q. Ding, Z. Kang, L. Cao, M. Lin, H. Lin and D.-P. Yang, Conversion of waste eggshell into difunctional Au/CaCO3 nanocomposite for 4-Nitrophenol electrochemical detection and catalytic reduction, *Appl. Surf. Sci.*, 2020, **510**, 145526.

15 Z. Hu, B. J. Deibert and J. Li, Luminescent metal–organic frameworks for chemical sensing and explosive detection, *Chem. Soc. Rev.*, 2014, **43**, 5815–5840.

16 B. Wang, X.-L. Lv, D. Feng, L.-H. Xie, J. Zhang, M. Li, Y. Xie, J.-R. Li and H.-C. Zhou, Highly Stable Zr(IV)-Based Metal–Organic Frameworks for the Detection and Removal of Antibiotics and Organic Explosives in Water, *J. Am. Chem. Soc.*, 2016, **138**, 6204–6216.

17 A. Mukhopadhyay, S. Jindal, G. Savitha and J. N. Moorthy, Temperature-Dependent Emission and Turn-Off Fluorescence Sensing of Hazardous "Quat" Herbicides in Water by a Zn-MOF Based on a Semi-Rigid Dibenzochrysene Tetraacetic Acid Linker, *Inorg. Chem.*, 2020, **59**, 6202–6213.

18 X. Zhang, G. Ren, M. Li, W. Yang and Q. Pan, Selective Detection of Aromatic Nitrophenols by a Metal–Organic Framework-Based Fluorescent Sensor, *Cryst. Growth Des.*, 2019, **19**, 6308–6314.

19 S. S. Saini, G. J. Copello and A. L. J. Rao, HPLC-UV platform for trace analysis of three isomeric mononitrophenols in water with chitin based solid phase extraction, *Anal. Methods*, 2017, **9**, 4143–4150.

20 J. Zhang, S. Cui, Y. Ding, X. Yang, K. Guo and J.-T. Zhao, Two-dimensional mesoporous ZnCo2O4 nanosheets as a novel electrocatalyst for detection of o-nitrophenol and p-nitrophenol, *Biosens. Bioelectron.*, 2018, **112**, 177–185.

21 D. Balram, K.-Y. Lian and N. Sebastian, Ultrasound-assisted synthesis of 3D flower-like zinc oxide decorated fMWCNTs for sensitive detection of toxic environmental pollutant 4-nitrophenol, *Ultrason. Sonochem.*, 2020, **60**, 104798.

22 C. Zhang, S. Govindaraju, K. Giribabu, Y. S. Huh and K. Yun, AgNWs-PANI nanocomposite based electrochemical sensor for detection of 4-nitrophenol, *Sens. Actuators, B*, 2017, **252**, 616–623.

23 M. Moradi, Y. Yamini, J. Kakehmam, A. Esrafili and M. Ghambarian, A new strategy to simultaneous microextraction of acidic and basic compounds, *J. Chromatogr. A*, 2011, **1218**, 3945–3951.

24 A. Peñalver, E. Pocurull, F. Borrull and R. M. Marcé, Solid-phase microextraction coupled to high-performance liquid chromatography to determine phenolic compounds in water samples, *J. Chromatogr. A*, 2002, **953**, 79–87.

25 M. Liu, Z. Gao, Y. Yu, R. Su, R. Huang, W. Qi and Z. He, Molecularly Imprinted Core-Shell CdSe@SiO 2/CDs as a Ratiometric Fluorescent Probe for 4-Nitrophenol Sensing, *Nanoscale Res. Lett.*, 2018, **13**, 27.

26 T. Liu, N. Li, J. X. Dong, Y. Zhang, Y. Z. Fan, S. M. Lin, H. Q. Luo and N. B. Li, A colorimetric and fluorometric dual-signal sensor for arginine detection by inhibiting the growth of gold nanoparticles/carbon quantum dots composite, *Biosens. Bioelectron.*, 2017, **87**, 772–778.

27 J. Li, D. Kuang, Y. Feng, F. Zhang, Z. Xu and M. Liu, A graphene oxide-based electrochemical sensor for sensitive determination of 4-nitrophenol, *J. Hazard. Mater.*, 2012, **201–202**, 250–259.

28 C. Zhang, S. Govindaraju, K. Giribabu, Y. S. Huh and K. Yun, AgNWs-PANI nanocomposite based electrochemical sensor for detection of 4-nitrophenol, *Sens. Actuators, B*, 2017, **252**, 616–623.

29 J. M. Gonçalves, P. R. Martins, D. P. Rocha, T. A. Matias, M. S. S. Julião, R. A. A. Munoz and L. Angnes, Recent trends and perspectives in electrochemical sensors based on MOF-derived materials, *J. Mater. Chem. C*, 2021, **9**, 8718–8745.

30 D. K. Yadav, V. Ganesan, F. Marken, R. Gupta and P. K. Sonkar, Metal@MOF Materials in Electroanalysis: Silver-Enhanced Oxidation Reactivity Towards Nitrophenols Adsorbed into a Zinc Metal Organic Framework—Ag@MOF-5(Zn), *Electrochim. Acta*, 2016, **219**, 482–491.

31 Y. Shen, H. Yan, H. Guo, Y. Long and W. Li, Defect-rich hexagonal boron nitride for the simultaneous determination of 4-aminophenol and phenol, *Sens. Actuators, B*, 2020, **303**, 127248.

32 H. Rao, Electroanalytical Investigation of p-nitrophenol with Dual Electroactive Groups on a Reduced Graphene Oxide Modified Glassy Carbon Electrode, *Int. J. Electrochem. Sci.*, 2017, 1052–1063.

33 J. W. Shin, K. Eom and D. Moon, BL2D-SMC, the supramolecular crystallography beamline at the Pohang Light Source II, Korea, *J. Synchrotron Radiat.*, 2016, **23**, 369–373.

34 Z. Otwinowski and W. Minor, [20] Processing of X-ray diffraction data collected in oscillation mode, *Methods Enzymol.*, 1997, 307–326.

35 Z. Otwinowski, D. Borek, W. Majewski and W. Minor, Multiparametric scaling of diffraction intensities, *Acta Crystallogr., Sect. A: Found. Crystallogr.*, 2003, **59**, 228–234.

36 G. M. Sheldrick, SHELXT – Integrated space-group and crystal-structure determination, *Acta Crystallogr., Sect. A: Found. Adv.*, 2015, **71**, 3–8.

37 G. M. Sheldrick, Crystal structure refinement with SHELXL, *Acta Crystallogr., Sect. C: Struct. Chem.*, 2015, **71**, 3–8.

38 C. B. Hübschle, G. M. Sheldrick and B. Dittrich, ShelXle : a Qt graphical user interface for SHELXL, *J. Appl. Crystallogr.*, 2011, **44**, 1281–1284.

39 R. Khan, M. Pal, A. v. Kuzikov, T. Bulko, E. v. Suprun and V. v. Shumyantseva, Impedimetric immunosensor for detection of cardiovascular disorder risk biomarker, *Mater. Sci. Eng., C*, 2016, **68**, 52–58.

40 F. M. M. Tchieno and I. K. Tonle, p-Nitrophenol determination and remediation: an overview, *Rev. Anal. Chem.*, 2018, **32**(2), 20170019.